PROCEEDINGS OF SPIE

SPIEDigitalLibrary.org/conference-proceedings-of-spie

Performance and characterization of the SPT-3G digital frequency multiplexed readout system using an improved noise and crosstalk model

Montgomery, J., Anderson, A., Avva, J., Bender, A., Dobbs, M., et al.

J. Montgomery, A. J. Anderson, J. S. Avva, A. N. Bender, M. A. Dobbs, D. Dutcher, T. Elleflot, A. Foster, J. C. Groh, W. L. Holzapfel, D. Howe, N. Huang, A. E. Lowitz, G. I. Noble, Z. Pan, A. Rahlin, D. Riebel, G. Smecher, A. Suzuki, N. Whitehorn, "Performance and characterization of the SPT-3G digital frequency multiplexed readout system using an improved noise and crosstalk model," Proc. SPIE 11453, Millimeter, Submillimeter, and Far-Infrared Detectors and Instrumentation for Astronomy X, 114530X (13 December 2020); doi: 10.1117/12.2561537

SPIE.

Event: SPIE Astronomical Telescopes + Instrumentation, 2020, Online Only

Performance and characterization of the SPT-3G digital frequency multiplexed readout system using an improved noise and crosstalk model

J. Montgomery[a], A. J. Anderson[b,c], J. S. Avva[d], A. N. Bender[e,c], M. A. Dobbs[a,f], D. Dutcher[c,g], T. Elleflot[h], A. Foster[i], J. C. Groh[d], W. L. Holzapfel[d], D. Howe[j], N. Huang[d], A. E. Lowitz[c], G. I. Noble[a], Z. Pan[c,g], A. Rahlin[b,c], D. Riebel[j], G. Smecher[k], A. Suzuki[h], and N. Whitehorn[l] on behalf of the SPT-3G collaboration

[a]Department of Physics and McGill Space Institute, McGill University, 3600 Rue University, Montreal, Quebec H3A 2T8, Canada
[b]Fermi National Accelerator Laboratory, MS209, P.O. Box 500, Batavia, IL, 60510, USA
[c]Kavli Institute for Cosmological Physics, University of Chicago, 5640 South Ellis Avenue, Chicago, IL, 60637, USA
[d]Department of Physics, University of California, Berkeley, CA, 94720, USA
[e]High-Energy Physics Division, Argonne National Laboratory, 9700 South Cass Avenue., Argonne, IL, 60439, USA
[f]Canadian Institute for Advanced Research, CIFAR Program in Gravity and the Extreme Universe, Toronto, ON, M5G 1Z8, Canada
[g]Department of Physics, University of Chicago, 5640 South Ellis Avenue, Chicago, IL, 60637, USA
[h]Physics Division, Lawrence Berkeley National Laboratory, Berkeley, CA, 94720, USA
[i]Department of Physics, Center for Education and Research in Cosmology and Astrophysics, Case Western Reserve University, Cleveland, OH, 44106, USA
[j]University of Chicago, 5640 South Ellis Avenue, Chicago, IL, 60637, USA
[k]Three-Speed Logic, Inc., Victoria, B.C., V8S 3Z5, Canada
[l]Department of Physics and Astronomy, University of California, Los Angeles, CA, 90095, USA

ABSTRACT

The third generation South Pole Telescope camera (SPT-3G) improves over its predecessor (SPTpol) by an order of magnitude increase in detector number. The technology used to read out and control these detectors, digital frequency-domain multiplexing (DfMUX), is conceptually the same as used for SPTpol, but extended to accommodate more detectors. A nearly 5x expansion in the readout operating bandwidth has enabled the use of this large focal plane, and SPT-3G performance meets the forecasting targets relevant to its science objectives. However, the electrical dynamics of the higher-bandwidth system depart in significant ways from the characterization and models drawn from the previous generation of cameras. We present an updated derivation for electrical crosstalk in higher-bandwidth DfMUX systems, and identify two previously uncharacterized contributions to readout noise. The updated crosstalk and noise models successfully describe the measured crosstalk and readout noise performance of SPT-3G, and suggest improvements to the readout system for future experiments using DfMUX, such as the LiteBIRD satellite.

Keywords: SPT-3G, DfMUX, FDM, readout noise, crosstalk, CMB instrumentation

Send correspondence to J. Montgomery: Joshua.J.Montgomery@mcgillcosmology.ca

Millimeter, Submillimeter, and Far-Infrared Detectors and Instrumentation for Astronomy X, edited by Jonas Zmuidzinas, Jian-Rong Gao, Proc. of SPIE Vol. 11453, 114530X
 · doi: 10.1117/12.2561537

1. INTRODUCTION

The South Pole Telescope is a 10-meter telescope that observes the sky at microwave frequencies from the Amundsen-Scott Research Station at the geographic South Pole. It is currently equipped with the SPT-3G receiver, the third camera to be deployed on the telescopeSPT-3G is in its third year of surveying a 1,500 deg^2 field of the Cosmic Microwave Background (CMB), using a polarization-sensitive tri-chroic focal plane with 16,000 detectors [1]. The detectors are bolometric transition-edge sensors (TES), which are metal filaments held at sub-Kelvin temperatures in the transition between normal and superconducting states [2]. These detectors convert depositions of incident power to variations in device resistance, which are sensed by applying a voltage bias to the TES elements and measuring variations in current through the circuit. This methodology is sufficiently sensitive to detect O(10 aW) fluctuations in power. TES devices have been the standard for the past three generations of SPT receivers, and are common throughout the field of CMB instrumentation in part because they operate at or near the photon noise limit. For this reason, each subsequent generation of receiver on SPT has achieved improved sensitivity primarily by increasing the number of TES devices operated simultaneously: SPT-3G observes the sky with an order of magnitude more detectors than SPTpol, which was decommissioned in 2017.

One of the enabling technologies for increases in focal plane size is the multiplexed readout, which allows multiple TES detectors to be operated with a shared set of electronics. Without multiplexing, detector numbers would be quickly constrained by cryogenic cooling limitations and cost of the readout system. As detector numbers rapidly increase, improvements to multiplexing technology are necessary. A multiplexing readout system includes room-temperature signal processing and cryogenic electronics,and is characterized by the number of detectors that can be operated as a single module of shared electronics (the *mux factor*). SPT-3G employs a 68x mux design that is conceptually based on the 16x mux system used on SPTpol, but extends the design to higher multiplexing.

Electrical models used in the forecasting and design of SPT-3G were derived from the 16x mux predecessors, and make use of a number of approximations or assumptions that are no longer valid in the higher mux factor regime. Consequently, several parameters such as electrical crosstalk and readout noise are measurably worse than expected. The deviations from forecasted expectations remain either within target requirements (in the case of crosstalk), or insignificant with respect to scientific analysis (in the case of elevated readout noise). Nevertheless, they indicate an incomplete understanding of the system dynamics, which we seek to correct with the model updates presented here. In Section 2 we give a simplified description of the readout system while highlighting the relevant non-idealities. In Section 3 we derive updated analytic forms for the crosstalk in such systems. In Section 4 the observed and modeled readout noise is presented, as well as descriptions of two new mechanisms relevant to accurately modeling SPT-3G readout noise. These mechanisms are explored in more detail in Sections 5 and 6. Results from this updated set of electrical models are being used to inform specific design choices to improve existing instruments using this technology, and future instruments such as the LiteBIRD satellite telescope.

2. DIGITAL FREQUENCY-DOMAIN MULTIPLEXING

The need to multiplex is dictated by the requirement that TES devices be kept at sub-Kelvin temperatures ($\sim$270 mK in the case of SPT-3G). Without multiplexing, each detector would be connected to room temperature by a separate pair of conductors, producing a total heat load in excess of the cooling power of the coldest stage of SPT-3G. SPT-3G overcomes this limitation by using a multiplexing strategy known as frequency-domain multiplexing (FDM). The particular FDM designs used on the SPT cameras are known as fMUX, starting with the SPT-SZ camera in 2007, which used an analog frequency-domain multiplexing (AfMUX) system [14] and was superseded by the digital frequency-domain multiplexing (DfMUX) system deployed on the SPTpol instrument in 2011 [3]. SPT-3G uses the second generation of DfMUX readout, which was first introduced in [4]. The description given here will omit details not relevant for the specific crosstalk and noise model updates, but a detailed account of the modern DfMUX design, and full noise modeling, can be found in [5].

DfMUX preserves the independence of each TES bias, while limiting the number of cryogenic wires required, by applying the bias voltages as megahertz sinusoids (the *carriers*). In the previous generation of DfMUX

readout up to 16 of these carriers were distributed at frequencies between 200 kHz and 1.2 MHz, but in the higher mux designs up to 68 such carriers are used in a bandwidth up to 5.5 MHz. The individual carrier tones are summed together in room-temperature electronics to generate a composite waveform that can be transmitted to the sub-Kelvin stage over a single pair of conductors. That waveform is separated back into the component sinusoids at the sub-Kelvin stage, using a bank of cryogenic resonant filters [6]. Carrier frequencies are chosen to correspond to filter resonant frequencies, and each TES is embedded within a filter. This allows a bias at the proper frequency to be applied to the TES, while isolating it from bias voltages intended for other devices. As the TES detectors vary in resistance, they amplitude-modulate the associated carrier tone, generating a current waveform in which the sky signal is encoded. Each of these amplitude-modulated tones is then summed to make a single output waveform. The output waveform is sensed cryogenically using a superconducting quantum interference device (SQUID), before being amplified by conventional electronics and digitally demodulated to recover the independent sky signals incident on each TES. This operation is analogous to AM radio, and is shown schematically in Figure 1.

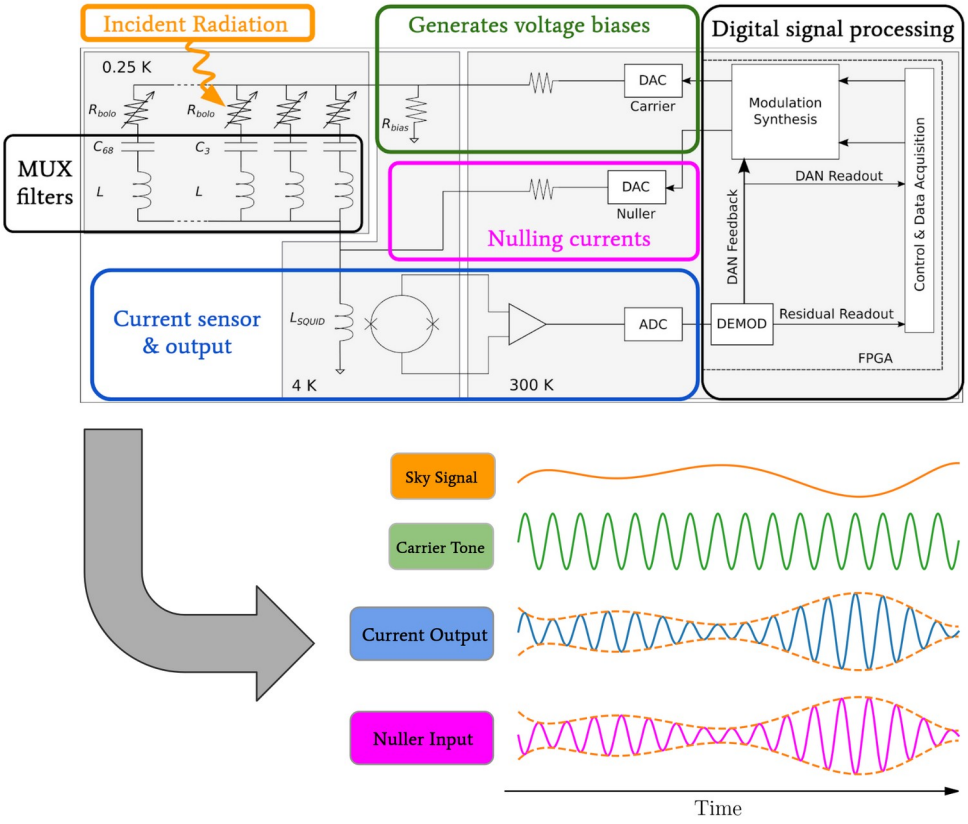

Figure 1: A simplified schematic diagram of the DfMUX readout system.Voltage biases are calculated and produced as a composite waveform in the warm electronics; these are divided back out into component sinusoids by a bank of cryogenic filters; incident radiation deposits power on the TES detectors, changing their resistance; this amplitude-modulates the carrier sinusoids and produces a current waveform with the sky signal encoded in the sidebands, similar to AM radio; the current waveforms are summed together into another composite waveform that is sensed in the output signal path. To linearize the SQUID amplifiers, a nulling waveform is generated that cancels signals at the input of the SQUID using active feedback. The nuller waveform is then used as the science data output, since it accurately reproduces the sky signal in order to cancel the current waveform. The lower inset figure shows example sky, carrier, output, and nuller signals for a single TES. Figure adapted from [7].

2.1 Nulling

SQUID devices are highly non-linear, and have a periodic response function and limited dynamic range (Figure 2). A typical SQUID of the type used on SPT-3G will generate non-single-valued outputs for inputs greater than ~2.1 μA, which is smaller than the current produced by a single TES voltage bias. To linearize the SQUID amplifiers, and enable their use, a separate current waveform is injected at the SQUID input to cancel the incoming signals. That current waveform is called a *nuller*, and is generated using narrow-band digital feedback centered at the carrier bias frequencies.The bandwidth of the feedback is sufficient to capture all science signals in the sidebands of the carrier tones; under this scheme our data is the signal generated by the feedback, rather than the output signal from the SQUID. This feedback system is known as Digital Active Nulling (DAN) and was first described in [8] for the first-generation DfMUX readout system. An account of DAN for modern higher-density systems can be found in [5].

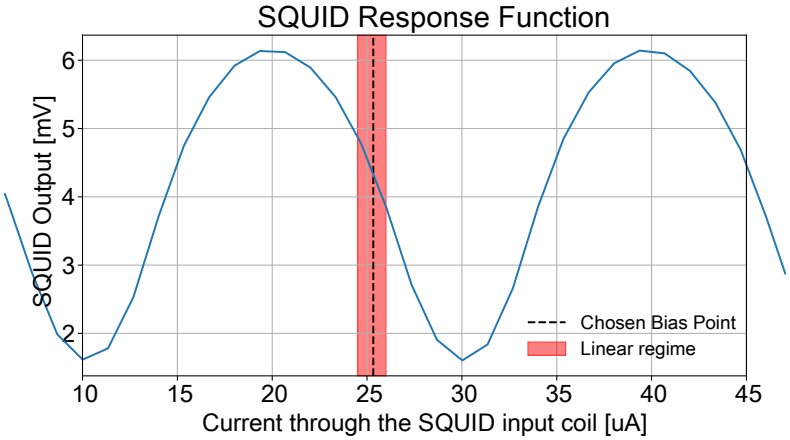

Figure 2: The SQUID output response is a periodic and non-single valued function of the input current, resulting in limited useful dynamic range. Annotated is the approximately linear response regime and the bias point at which we operate the SQUIDs. This bias point refers to a DC input bias (the *flux bias*) used to center the SQUID response in the linear regime. Figure from [5].

2.2 Parasitic capacitances to ground

The schematic readout diagram shown in Figure 1 lacks a few stray circuit elements of the system that have become relevant at the higher bias frequencies now used.The most notable of these are capacitances to ground within the cryogenic filtering elements. The filters themselves are made up of 2D lithographic devices that generate capacitance and inductance using geometric shapes.The shapes are etched with trace widths between 4 μm and 16 μm and total areas of up to approximately 20 mm^2[5, 9, 10]. A byproduct of this design is a parallel-plate capacitance with the ground plane 675 μm away.There are similar capacitances to ground throughout the readout electronics, formed by traces on the TES wafer and the separate PCBs on which the filters and SQUIDs are mounted. All of these may be estimated analytically based on the design of the lithography or layout of the electronics cards.

These capacitances to ground are largely irrelevant at lower bias frequencies, but at higher frequencies they present a low enough impedance path through the system to modify transfer functions significantly. This effect was first noted in [11] with respect to detector parameter estimation. We show in Section 6 that these parasitic current paths are also relevant to readout noise. A more complete circuit model for the synthesizer signal path is given in Figure 3.

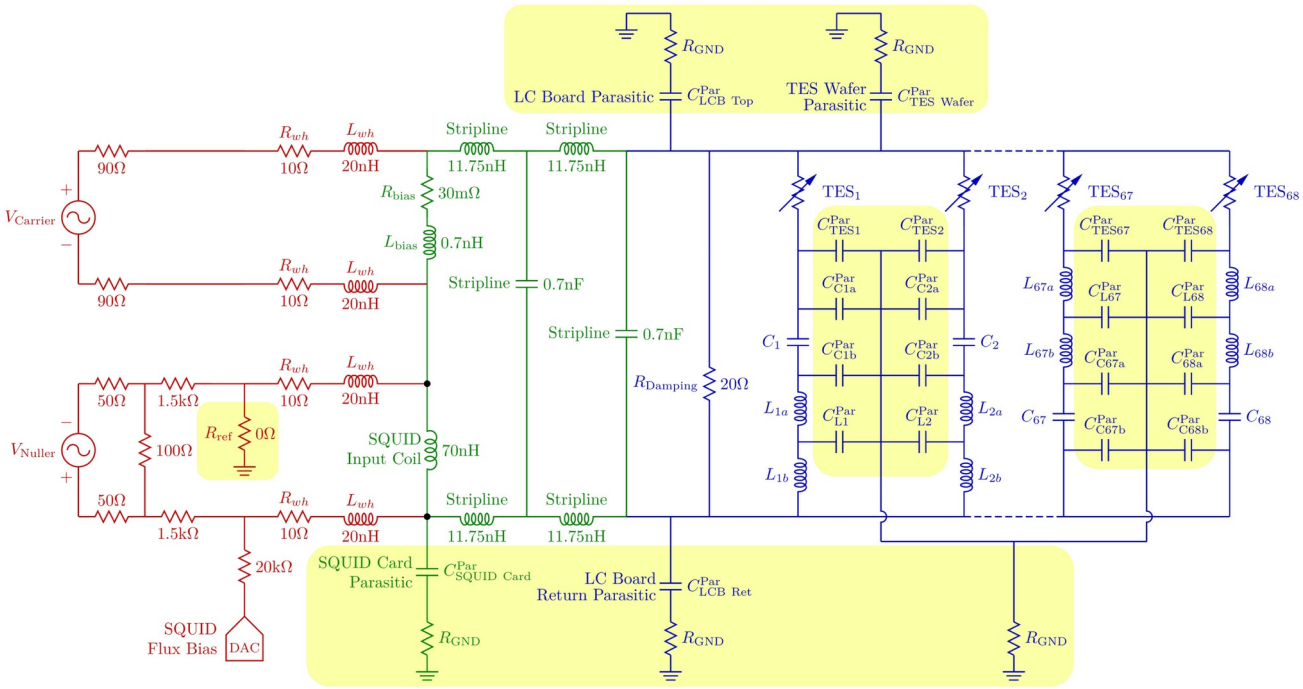

Figure 3: An electrical model of the signal chain that includes stray impedances, such as an inductance in series with the bias resistor [12], series inductance in the striplines [13], and parasitic capacitances to ground [5, 11]. Red corresponds to electronics at room temperature through to the wire-harness. Green corresponds to electronics at the 4K stage through to striplines that connect the 4K and sub-Kelvin stages. Blue indicates electronics at the sub-Kelvin stage that include the LC filtering board and TES wafer. Parasitic strays new to this circuit model and relevant to the discussions herein are highlighted in yellow. R_{GND} is typically low impedance. Channels 1 & 2 demonstrate the RCL configuration, while Channels 67 & 68 demonstrate an alternative RLC configuration that is also used for SPT-3G filters. Not pictured are the initial amplification or filtering stages common to both the carrier and nuller outputs or the output path between the SQUID output and the ADC.

3. CROSSTALK

Electrical coupling between detectors in a DfMUX system is typically the dominant source of crosstalk in the instrument. This can occur in two ways:

Leakage *current* crosstalk happens when the i^{th} carrier voltage is amplitude-modulated by variations in the n^{th} TES within a different filter. This is caused by overlap between the filter bandwidths, which allows some current to leak through one of the other parallel legs of the cryogenic filter. This effect is a strong function of the filter shape and spacing, and causes signal from the n^{th} TES to crosstalk into the output from the i^{th} TES.

Leakage *power* crosstalk happens because leakage current deposits electrical power across the TES in the legs it leaks through. Under some conditions, deposited power across the i^{th} TES due to leakage current can vary as a function of the i^{th} TES resistance. This varying leakage power mimics the power depositions from the sky, and causes signal from the i^{th} TES to crosstalk into the output from the n^{th} TES.

These mechanisms were first derived for an fMUX system in [14, hereafter Dobbs2012], and those derivations were used to model the expected crosstalk performance of the SPT-3G designWhile the mean crosstalk performance met our design requirement [4], the phenomenology diverges noticeably from the expectation. This is largely a

consequence of additional stray impedances relevant to crosstalk, which were not characterized or included in the Dobbs2012 derivations. A more complete derivation of these crosstalk mechanisms is given in Section 3.1. The resulting total crosstalk is described in Section 3.2, and Section 3.3 uses in-situ crosstalk measurements to validate the model updates. The primary differences with the Dobbs2012 model are

1. Inclusion of stray series resistance within each parallel leg of the LC filter network. This effect dominates differences between the two models for SPT-3G-like parameters, where leakage current crosstalk is amplified because of stray resistances.
2. Preservation of phase information. The Dobbs2012 model approximates the total crosstalk fraction using the magnitudes of each of the crosstalk and primary signals.However, these signals can all be significantly out-of-phase with one another, leading to cancellation and suppression. This effect is noticeable though relatively small for an SPT-3G-like design, but can be significant for systems with large series impedance with the cryogenic filters.
3. Bias frequency flexibility. The Dobbs2012 model assumes bias frequencies are exactly at the filter resonance. In higher-bandwidth systems, it is common for bias frequencies to be offset from the true resonant frequency by up to a few hundred hertz, inducing extra complex impedance. These offsets are due to fluctuations in the resonant frequencies as a function of TES resistance, and how bias frequencies are chosen to mitigate inter-modulation distortion products [5].

3.1 Crosstalk model derivation

The simplified circuit model shown in Figure 4 sufficiently captures the relevant electrical elements for calculating crosstalk:

1. A voltage source producing carrier sinusoids at frequencies ω
2. The filtering network, formed by a parallel bank of series LCR filters. Each leg of the filter includes both a TES and a stray series resistance.
3. A common impedance in series with the filtering network. In the SPT-3G system this is dominated by the inductive reactance of the cryogenic striplines between the 4K and sub-Kelvin stages.

The circuit model omits the nulling path or the parasitic capacitances. The nulling path modifies Z_{com} to remove the SQUID input impedance in series with the cryogenic filter, which is equivalent to a different choice of Z_{com}. Parasitic capacitances can modify the effective impedance of the parallel legs, but the variation is small relative to other sources of impedance and doesn't meaningfully change crosstalk dynamics. Typical SPT-3G parameters for the elements in this circuit model are summarized in Table 1.

Following Figure 4, for bias frequency ω, the impedance of any single cryogenic filter leg n is

$$Z_{n,i} = R_{\mathrm{TES},n} + r_{s,n} + j\omega_i L_n + \frac{1}{j\omega_i C_n}, \tag{1}$$

such that $R_{\mathrm{TES},n}$ is the TES resistance, r_s is any stray series resistance with the TES, and L and C are the inductor and capacitor elements that define the filter resonant frequencies. In this notation the impedance of the *on-resonance* cryogenic leg is $Z_{i,i}$, while $Z_{n6=i,i}$ are the impedances of *off-resonance* cryogenic legs. The impedance of the full parallel network is

$$Z_{\mathrm{net}}(\omega_i) = \left(\sum_{n=1}^{\mathrm{muxFactor}} \frac{1}{Z_{n,i}} \right)^{-1}. \tag{2}$$

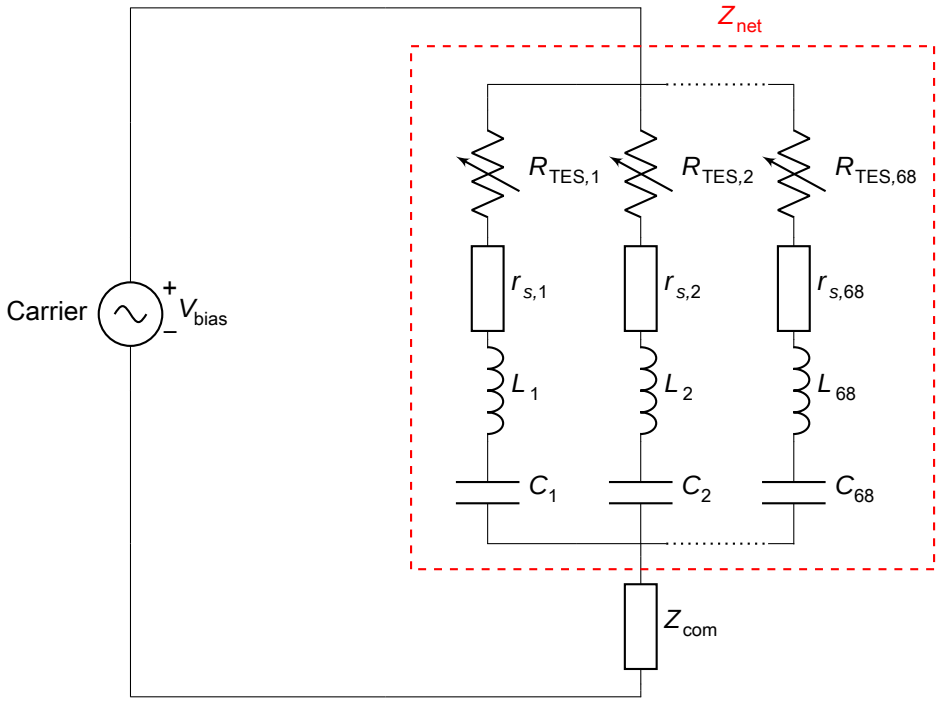

Figure 4: An example circuit diagram of the cryogenic network. This includes all relevant components used in the derivation of leakage current crosstalk and leakage power crosstalk.

Typical SPT-3G Parameters

Parameter	Value
Z_{com}	$j\omega\cdot$(46 nH)
R_{TES}	1.3 Ω to 1.7 Ω
R_s	0.25 Ω to 0.4 Ω
L	60 μH
C	12 pF to 150 pF
$2\pi\omega$	1.6 MHz to 5.5 MHz, log-spaced

Table 1: Typical SPT-3G circuit parameters relevant to the calculation of electrical crosstalk. Resonant frequencies are designed by varying the capacitance to distribute the frequencies logarithmically within the bandwidth, so the lowest frequency regime has the narrowest frequency spacing. Bias frequencies are selected based on the resonant frequencies exhibited, but may be offset from the exact resonant frequency by up to several hundred hertz.

$i \pm 1$ are *nearest-neighbors* with respect to i, such that $Z_{i\pm1,i}$ are the two lowest impedance paths through the cryogenic network at ω_i aside from the on-resonance leg.* Significant crosstalk coupling only occurs between on-resonance detectors and nearest-neighbors. For SPT-3G design parameters, $Z_{i\pm1,i}$ ranges from 20 to 80 Ω, while $Z_{i,i}$ are typically <2 Ω. Therefore, the impedance of the network at each bias frequency may be approximated

$$Z_{\text{net}}(\omega_i) \approx Z_{i,i} \,. \tag{3}$$

3.1.1 Primary signal

The intended primary signal is the change in current at frequency ω_i due to changes in the on-resonance TES resistance $R_{\text{TES},i}$:

$$\left.\frac{\delta I_i}{\delta R_{\text{TES},i}}\right|_{\text{signal}} = \frac{\delta}{\delta R_{\text{TES},i}} \frac{V_{\text{bias}}(\omega_i)}{Z_{i,i} + Z_{\text{com}}(\omega_i)} \tag{4}$$

$$\delta I_{i,\text{signal}} = \frac{-V_{\text{bias}}(\omega_i) \cdot \delta R_{\text{TES},i}}{(Z_{i,i} + Z_{\text{com}}(\omega_i))^2} \,. \tag{5}$$

Crosstalk happens when $\left.\frac{\delta I_i}{\delta R_{\text{TES},n\neq i}}\right| \neq 0$.

3.1.2 Leakage current crosstalk

Leakage current crosstalk occurs because some fraction of the current induced through Z_{net} by $V_{\text{bias}}(\omega_i)$ flows through an off-resonance leg $n \neq i$, allowing variations in an off-resonance TES to amplitude-modulate $V_{\text{bias}}(\omega_i)$ in a similar way to the on-resonance TES. This form of crosstalk is given by

$$\left.\frac{\delta I_i}{\delta R_{\text{TES},n\neq i}}\right|_{\text{LCX}} = \frac{\delta}{\delta R_{\text{TES},n}} \frac{V_{\text{bias}}(\omega_i)}{(Z_{n,i} + Z_{\text{com}}(\omega_i))} \,. \tag{6}$$

Expressed as a leakage current signal, $\delta I_{i,n,\text{LCX}}$, this becomes

$$\delta I_{i,n,\text{LCX}} = \frac{-V_{\text{bias}}(\omega_i) \cdot \delta R_{\text{TES},n}}{(Z_{n,i} + Z_{\text{com}}(\omega_i))^2} \,. \tag{7}$$

Or as a crosstalk fraction, using Equation 5,

$$\frac{\delta I_{i,n,\text{LCX}}}{\delta I_{i,\text{signal}}} = \frac{\delta R_{\text{TES},n}}{\delta R_{\text{TES},i}} \left(\frac{Z_{i,i} + Z_{\text{com}}(\omega_i)}{Z_{n,i} + Z_{\text{com}}(\omega_i)}\right)^2 \,. \tag{8}$$

For most practical systems $\delta R_{\text{TES},n} \approx \delta R_{\text{TES},i}$ and the first term drops out. Variations in TES resistance produce signals in a very narrow bandwidth relative to the filter bandwidths, so crosstalk fractions calculated at the bias frequencies are sufficient to describe the crosstalk across all sideband signals of interest. Note that common impedances to the filtering network (Z_{com}) contribute to leakage current crosstalk, but are not required for it.

3.1.3 Leakage power crosstalk

Leakage current dissipates power across the TES detectors in the off-resonance legs through which it flows; this is called *leakage power*. Leakage power deposited onto the i^{th} detector from leakage current induced by the n^{th} voltage bias is given by

$$P_{i,n} = \left(\frac{Z_{\text{net}}(\omega_n) V_{\text{bias}}(\omega_n)}{Z_{\text{net}}(\omega_n) + Z_{\text{com}}(\omega_n)}\right)^2 \frac{R_{\text{TES},i}}{Z_{i,n}^2} \,. \tag{9}$$

* This notation implies that nearest-neighbors are always those immediately adjacent in frequency-space to the primary leg, i. In practice this is nearly always true, but in principle the two lowest-impedance paths through off-resonance filter legs can both have lower resonant frequencies, or higher resonant frequencies, than the on-resonance path.

In the simple case when $Z_{com} = 0$, leakage power deposited across any TES is only a function of that TES resistance, and therefore no crosstalk mechanism exists. When $Z_{com} \neq 0$, an additional voltage divider is formed with the cryogenic network, converting the fixed voltage bias across the filtering network into one that is a function of the network impedance at ω_n. Variations in $R_{TES,n}$ then modulate $P_{i,n}$, generating a form of crosstalk

$$\left.\frac{\delta I_i}{\delta R_{TES,n\neq i}}\right|_{LPX} = \frac{1}{V_{bias}(\omega_i)} \frac{\delta P_{i,n}}{\delta R_{TES,n}} . \quad (10)$$

Expressed as a leakage power signal, $\delta I_{i,n,LPX}$, this becomes

$$\delta I_{i,n,LPX} \approx \frac{V^2_{bias}(\omega_n)}{V_{bias}(\omega_i)} \frac{Z_{n,n} Z_{com}(\omega_n)}{(Z_{n,n} + Z_{com}(\omega_n))^3} \left(\frac{2 R_{TES,i} \delta R_{TES,n}}{Z^2_{i,n}}\right) , \quad (11)$$

with the approximation from Equation 3 applied. The equation in the form of a crosstalk fraction is

$$\frac{\delta I_{i,n,LPX}}{\delta I_{i,signal}} \approx - \frac{V^2_{bias}(\omega_n)\delta R_{TES,n}}{V^2_{bias}(\omega_i)\delta R_{TES,i}} \frac{(Z_{i,i} + Z_{com}(\omega_i))^2}{(Z_{n,n} + Z_{com}(\omega_n))^3} \left(\frac{2 R_{TES,i} Z_{n,n} Z_{com}(\omega_n)}{Z^2_{i,n}}\right) . \quad (12)$$

This expression simplifies under the reasonable assumption that the detectors are approximately uniform in resistance and saturation power (and therefore bias voltage), in which case the first term drops out.

3.2 Total crosstalk fraction

The expressions for each signal described above have significant (and different) imaginary components, indicating they are all shifted in phase with respect to one another. All DfMUX systems record the complex signature of I_i, and the phase of the primary signal $I_{i,signal}$ is separately measured in-situ as part of the calibration for each observation.[†] The final data product in the time domain is the projection of I_i in-phase with the primary signal $I_{i,signal}$ [5]. The total crosstalk fraction is therefore the vector sum of two out-of-phase copies of the crosstalk signal, which partially cancel, which is then further suppressed as it is projected into the primary signal axis. This is shown in Figure 5, where the two figures indicate the phase and magnitudes of each signal, and in Figure 6, where the effective crosstalk along the primary signal axis is plotted. Figure 6 shows how the Dobbs2012 model underestimates leakage current crosstalk (due to the contribution from r_s) and overestimates leakage power crosstalk (at low frequencies, due to suppression when projected along the primary signal axis).

The crosstalk cancellation may seem non-intuitive, but it makes sense qualitatively: a decrement in the n^{th} TES resistance will generate an *increment* in the current at ω_i (due to leakage current crosstalk), but it will also increment the deposited leakage power across the i^{th} TES, raising its resistance, and causing a *decrement* in current at ω_i (due to leakage power crosstalk).These forms of crosstalk therefore oppose one another, though not perfectly, due to a phase offset in their action.

3.3 Crosstalk model validation

Measurements of crosstalk in-situ using optical sources have been previously described in [4]. Comparison between these measurements and electrical crosstalk modeling is limited by systematic offsets due to contributions from optical crosstalk, the precision of the optical measurements, and the fact that such measurements can only be done between detectors that have sufficiently different beams on the sky (so the crosstalk image can be distinguished from the source image). The design of the focal plane wiring is intended to minimize the beam offsets between nearest-neighbors,so detector pairs with the most crosstalk also observe nearly the same part of the sky. This makes it difficult to measure most nearest-neighbor crosstalk using optical measurements. Consequently, the best statistical test of the crosstalk is in the basis of bias frequency *separation*, rather than by bias frequency, as in Figure 7. The region of low frequency separation allows an easy differentiation between the two crosstalk models. Channel pairs with frequency separations narrower than the minimum designed spacing of 29 kHz are due to statistical scatter in the fabricated filter resonances. Though not an ideal comparison, the result indicates the importance of stray impedances in crosstalk calculations.

[†]More precisely, the phase of I_i is measured in-situ, but because the total crosstalk fraction is very low this is a good approximation of the phase of $I_{i,signal}$.

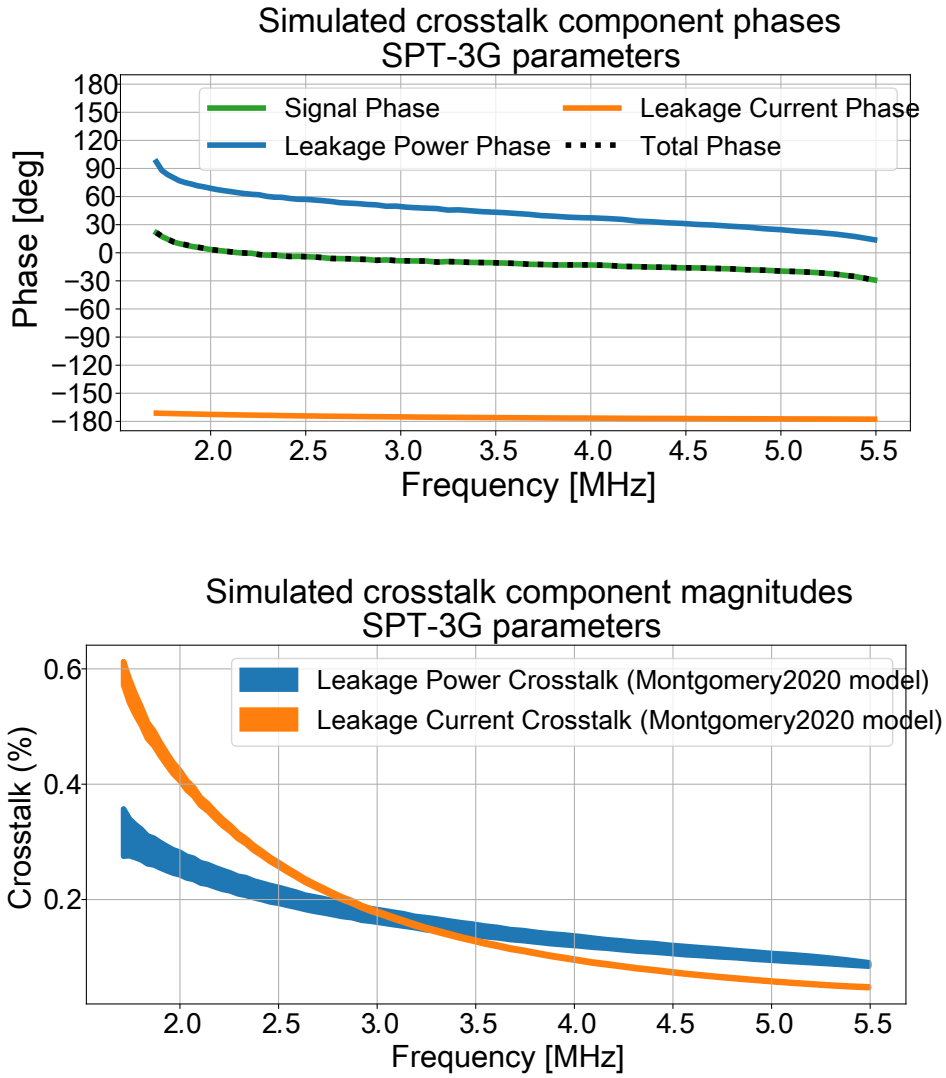

Figure 5: **Top:** The phase of each crosstalk component for a simulated SPT-3G multiplexing module with typical properties. The phases $\delta I_{i,\mathrm{signal}}$ and δI_i are nearly identical because the total crosstalk fraction is very low. Most striking, the relative phase offset between the leakage power and the primary signal ranges from between approximately 90° and 45°, suppressing the effective contribution of leakage power crosstalk. **Bottom:** The magnitudes of each crosstalk component for an SPT-3G-like system.The line widths indicate the difference between $(i, i-1)$ and $(i, i+1)$ nearest-neighbor pairsBecause they are nearly 180° out of phase, these contributions largely cancel. Furthermore, only the *projection* of these magnitudes aligned with the signal phase will contaminate the data. The widths of the shaded areas reflect differences in the crosstalk fraction between the two nearest-neighbors at each TES bias frequency.

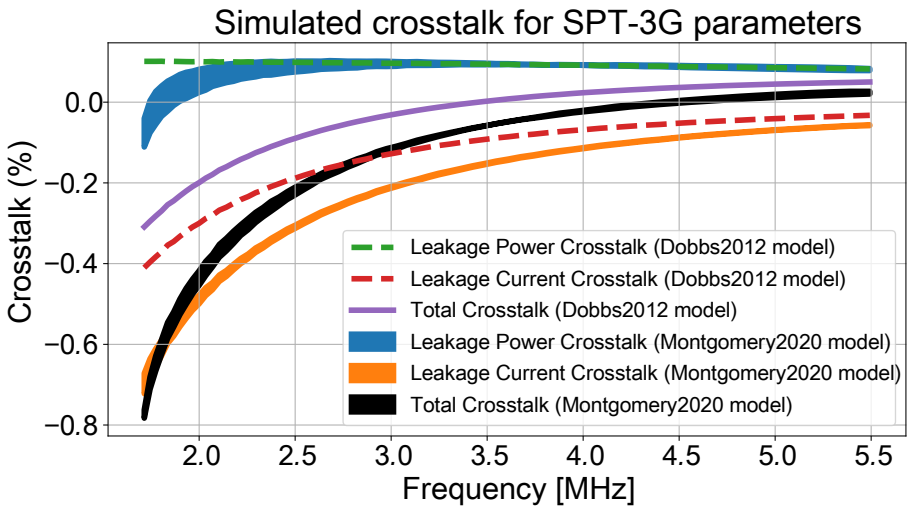

Figure 6: A comparison of the effective crosstalk fractions for a multiplexing module with typical SPT-3G parameters. Each mechanism is calculated via the derivations provided here and from Dobbs2012.The stray series resistance s is responsible for a larger leakage current contribution than calculated using the Dobbs2012 derivations. The dip in leakage power crosstalk at low frequency is due to the increased suppression from a $\sim 90^\circ$ phase offset relative to the primary signal. The Dobbs2012 model is largely insensitive to differences between (i, $i-1$) and (i, $i+1$) nearest-neighbor pairs and so has no visible changes in line width.

4. READOUT NOISE MODELING UPDATE

Instrument noise can be considered in two categories:

Detector noise: fundamental noise sources intrinsic to the TES operation and incident radiation. This category includes the photon noise (arrival time statistics of incident photons [15]) and phonon noise (random motion of thermal carriers that move heat away from the TES [16]). These noise sources deposit power on the TES detector, which is converted to a current noise via the detector *responsivity* (S, in units of $\frac{\text{pA}}{\text{aW}}$).

Readout noise: current noise sources that are additive with respect to the first category, and independent of the detector responsivity. These are conventionally characterized as a noise equivalent current (NEI) spectral density in units of $\frac{\text{pA}}{\sqrt{\text{Hz}}}$ at the SQUID input. Sources of readout noise include: SQUID output noise, amplifier noise, transistor noise in the Digital-to-Analog converters (DACs) and Analog-to-Digital Converters (ADCs), Johnson-Nyquist noise from Ohmic elements in the signal path, and quantization noise from the digitization. [‡] For the purposes of this discussion, TES Johnson noise is also included as a readout noise source. When the detectors are operating this is heavily suppressed, but when we measure readout noise as below it is not [17].

Readout noise can be measured in-situ when detectors are saturated, such that detectors are in the fully normal state and have no responsivity to incident power ($S = 0$), thereby disabling non-readout noise sources. Individual readout noise sources, defined for predecessor systems in [14], remain largely the same in higher-bandwidth implementations. Despite this, NEI predictions based on the models used for previous generations of DfMUX systems poorly reconstruct the observed readout noise at higher bias frequencies. We identify two new effects that modulate the effective amplitude of the existing noise sources and resolve this inconsistency. Both of these effects occur due to parasitic impedances in the electronic circuit that only become relevant at higher

[‡] A detailed breakdown of these noise sources for SPT-3G can be found in [5].

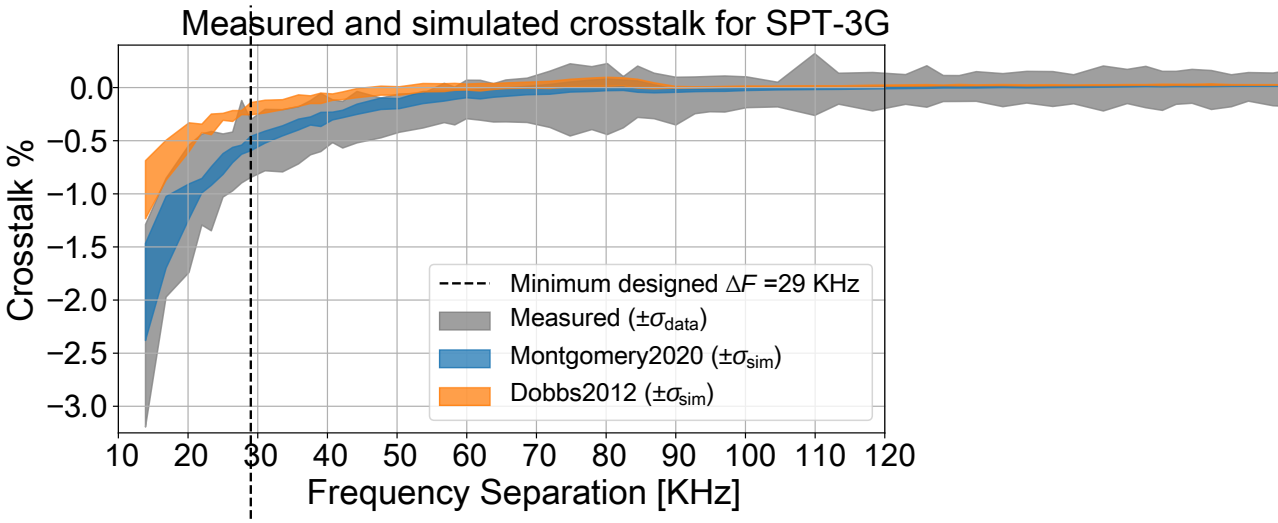

Figure 7: Shown above is a comparison between measured in-situ crosstalk and simulated crosstalk for 4,400 detector pairs in the receiver. Each pair differs slightly in r_s, R_{TES}, and underlying bias frequencies. These have been measured separately and serve as inputs to the simulations. Since these variations are all binned together according to frequency separation, some variance in the crosstalk distributions within each bin is expected. Shown here are the 1σ distributions in the measured and simulated crosstalk values, binned with equal-weight binning. It is clear the blue model (Montgomery2020), which includes stray impedances, is a better approximation for the measured crosstalk (gray) than the Dobbs2012 model (orange), which omits stray impedances. The narrower distribution of the Montgomery2020 values may be indicating an additional source of variation not captured in the model, or may reflect the imprecision of individual measurements of in-situ crosstalk from optical sources. The width of the measured distribution at the highest frequency separations favors the latter interpretation.

signal frequencies. With this new understanding, minor hardware changes can be made to reduce or eliminate this noise in future implementations.

An effective low-pass output filter between the SQUID output and the room-temperature amplification stages. This filter attenuates signal but not a subset of the readout noise sources in the output signal path, effectively amplifying that subset of readout noise sources when referred back through the filter to the SQUID input. In this sense it is a typical transfer function effect, but had been unrecognized previously. This output filter is described in more detail in Section 5.

Parasitic capacitances to ground in the cryogenic electronics, which generate a *current sharing* effect like the one first characterized in [7]. In [7], a current path was identified in which signals avoided the SQUID input by flowing back through the cryogenic filter network. Here we identify a second current path that bypasses the SQUID input, this time via parasitic capacitances to ground throughout the readout system. Similarly to the output filter effect, this results in an amplification of noise sources in the output signal path between the SQUID and ADC, but unlike the output filter it also applies to the intrinsic SQUID noise. The resulting noise increase can be determined analytically based on the cryogenic electronics design. Section 6 details this new current sharing path. Another byproduct of this current path is that it partially spoils the differential balancing of the transmission lines going into the cryostat, making them more susceptible to radio frequency interference (RFI) pickup.

A full circuit model that includes both of these effects forms the core of an updated noise model used to calculate noise expectations of the SPT-3G receiver. Figure 8 shows the measured readout noise alongside the

previous noise model and the updated noise model. Besides describing the observed SPT-3G readout noise, this model suggests two methods for improving noise performance in SPT-3G or future DfMUX readout designs, such as for LiteBIRD. These are covered in the individual sections below as part of the verification of each effect.

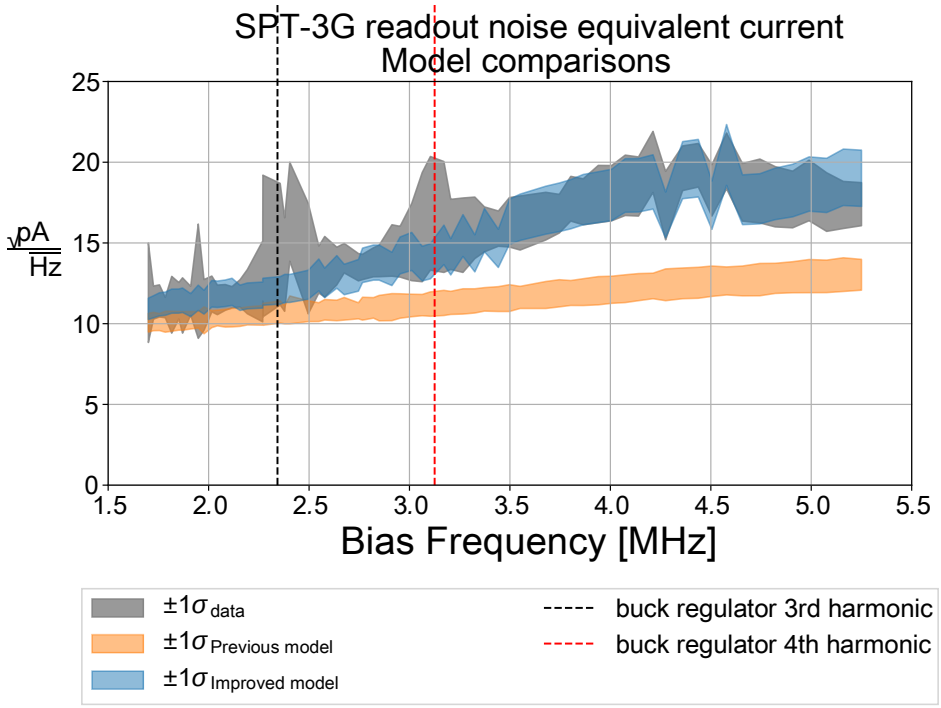

Figure 8: A comparison of measured SPT-3G readout noise with the previous noise model (orange) and an updated model (blue). The updated model includes the effect of parasitic capacitances relevant to current sharing and the output filter generated by the SQUID dynamic impedance. The width of the distributions are calculated from the standard deviation of noise realizations for each bias frequency within every multiplexed module, based on the distribution of measured SQUID parameters such as dynamic impedance and transimpedance. Variation in SQUID performance is responsible for most of the scatter between detectors operated at the same bias frequencies. Dotted lines indicate the approximate switching frequencies of the buck regulators used to generate power in the warm electronics, and are a known source of additional noise not specifically captured in the noise model. Discontinuous steps as a function of bias frequency, most prominent at 4.5 MHz, are due to changes in the geometric properties of the lithographic cryogenic filters for each resonator [5], and captured in the updated circuit model.

5. OUTPUT FILTER

The signal path relevant to the output filter is between the SQUID output and the first room-temperature amplification stage, shown in Figure 9. An interaction between the SQUID dynamic impedance (Z_{dyn}) and a parallel capacitance in the wire harness (C_{wh}) generates a low-pass filter with a cutoff frequency $f_c \sim \frac{1}{2\pi Z_{dyn} C_{wh}}$. The SQUID dynamic impedance characterizes the relationship between the SQUID output voltage and current through the Josephson junctions that form the SQUID output, [18]

$$Z_{dyn} = \frac{\delta V_{out}}{\delta I_{jj}}. \quad (13)$$

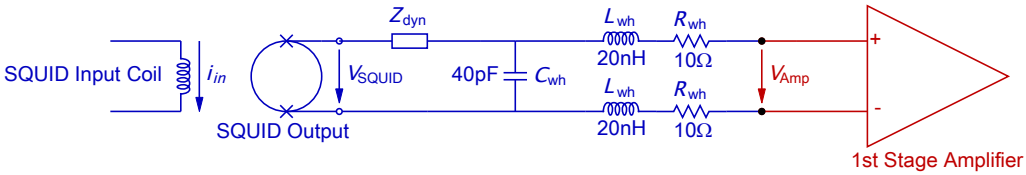

Figure 9: The cryogenic portion of the output signal path is shown here in blue. An important interaction between C_{wh} and Z_{dyn} forms a low-pass filter that attenuates high frequency signals before they reach the 1st stage amplifier input.

It is a SQUID property that is easily measured, and can be modeled as a real resistance in series with the voltage output signal. The transfer function describing the resulting attenuation of the voltage signals is defined as $\chi_{output} = \frac{V_{Amp}}{V_{SQUID}}$.

The value of approximately 40 pF for C_{wh} is empirically determined, and consistent with data-sheet values for the wire harness design of approximately 18 cm of 38 AWG manganin twisted pair. SPT-3G uses NIST SA13 SQUIDs with median dynamic impedance of approximately 750 Ω, although there are six outliers that are operated in a low dynamic impedance configuration of approximately 350 Ω. Figure 10 shows the resulting χ_{output} for each detector in the SPT-3G receiver, inferred based on measurements of C_{wh} and Z_{dyn}.

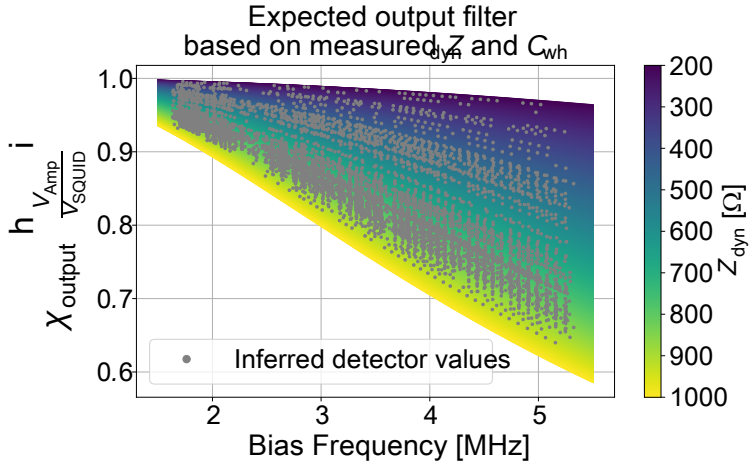

Figure 10: An analytic calculation of the output filter (χ_{output}) as a function of SQUID dynamic impedance (Z_{dyn}) for the measured value of C_{wh} =40 pF. Grey points indicate inferred values for each detector in the receiver, showing that some detectors benefit from low dynamic impedance SQUIDs, but most detectors are significantly affected, especially at high bias frequency. Noise sources in the output signal path are referred to an NEI at the SQUID input by dividing by χ_{output}, and therefore appear *amplified* by this filter.

The role of this output filter on the readout noise performance is shown using the six SQUIDs in SPT-3G operated with low dynamic impedance. Figure 11 shows that measured readout noise for detectors associated with the low dynamic impedance SQUIDs is significantly lower than the receiver distribution, and consistent with an expectation generated from the noise model that assumes all SQUIDs exhibited similar 350 Ω dynamic impedance.

In principle, all SQUIDs in the SPT-3G receiver can be operated with lower dynamic impedance; however, in nearly all cases such operation results in worse overallperformance. This performance degradation is likely a consequence of the milder output filter, which fails to attenuate out-of-band resonances or signals as strongly,

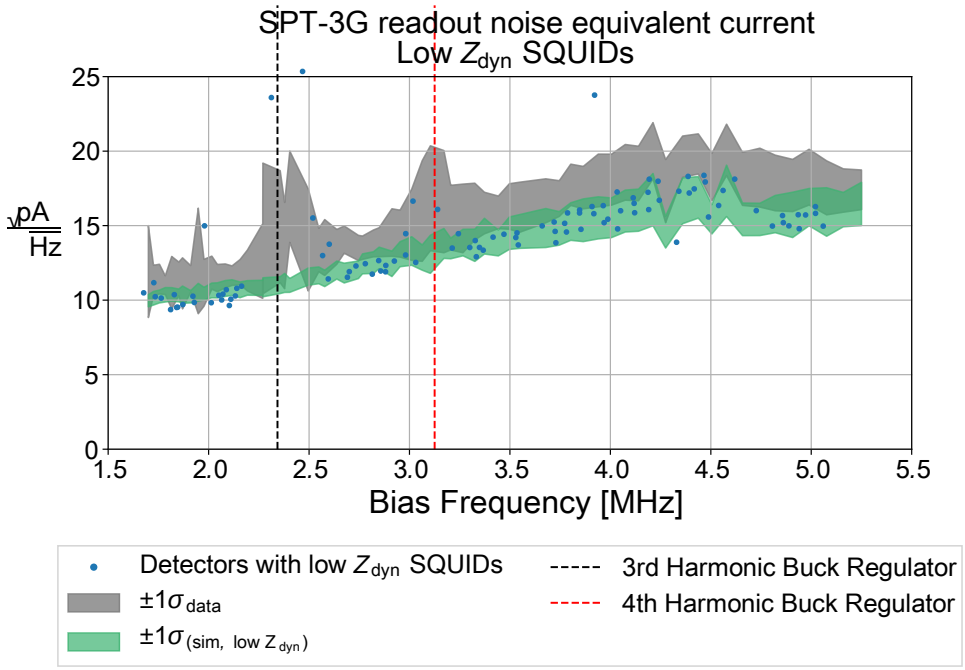

Figure 11: Measured readout noise in detectors operated with SQUIDs exhibiting a lower dynamic impedance (blue points above) is systematically lower than the rest of the receiver (shown in gray as in Figure 8). This difference is consistent with the expectation from the noise model, which predicts a ~ 10% noise improvement at high frequency from lower dynamic impedance SQUIDs. This model is shown in green, where low Z_{dyn} operation of the entire receiver is simulated. There are currently 6 SQUIDs on SPT-3G operated at low Z_{dyn}.

which then couple back into the SQUID input [5]. It's not clear why the six SQUIDs identified above do not exhibit degraded performance in this configuration, as they are otherwise of the same design. It may be possible to operate all SQUIDs in the SPT-3G receiver in such a configuration, but a ~10% improvement in readout noise corresponds to a negligible improvement in mapping speed for SPT-3G as a whole. Therefore the utility in the low dynamic impedance operation described above is primarily as a strong test of the noise model presented here.

6. CURRENT SHARING

Recall from Section 2.1 that Digital Active Nulling uses feedback in discrete bandwidths centered at the carrier frequencies to minimize signals at the digital demodulation stage (labeled "DEMOD" in Figure 1). DAN injects whatever current necessary to achieve this into the SQUID input. In most cases this is equivalent to minimizing the signal at input of the SQUID, which is the intended outcome: currents injected by the nuller that cancel signals that physically exist at the SQUID input do so by perfectly matching the amplitude of those signals at the SQUID input, thereby both canceling and faithfully recording them. However, noise sourced between the SQUID output and the ADC (the *output path*) is not physically present at the input of the SQUID. In response to such signals DAN will drive current *through* the SQUID to generate opposing voltages at the digital demodulation stage. Nulling currents that do not cancel existing physical signals have several parallel paths through which to return, and only one of these is through the SQUID input. A fraction of the delivered waveform then flows *around* the SQUID input through these other parallel paths. Only current flowing through the SQUID input will cancel signals generated in the output signal path, so DAN must produce a larger copy of that noise to compensate for the portion lost via the parallel paths. We are unable to distinguish between noise sources in our data, and so this is equivalent to a transfer function effect that amplifies noise sources in the output path, including the intrinsic SQUID noise.

The term given to the mechanism by which current is diverted around the SQUID input is *current sharing*, and the factor by which noise sources in the output path are amplified by this process is the *current sharing factor*. Following the circuit shown in Figure 3, the three current paths that define the magnitude of this effect are

1. Through the SQUID input coil ($|j\omega L_{squid}| \sim 2.3\Omega$ at the highest bias frequencies) and back through the wire-harness ($|R_{wh} + j\omega L_{wh}| \sim 10\Omega$), for a total of $O(10\ \Omega)$. This is the desired current path, and ideally is the lowest impedance option to limit the current sharing factor in the system.
2. Through the striplines ($Z_{com} \sim 0.5\Omega$ at optimal bias frequencies), across the filtering network ($Z_{net} \sim 1.7\Omega$), through the low impedance leg that generates the bias voltage ($|R_{bias} + j\omega L_{bias}| << 1\Omega$), and back out through the wire-harness ($|R_{wh} + j\omega L_{wh}| \sim 10\Omega$), for a total of $O(10\ \Omega)$. This path shares the final leg through the wire harness with (1). If this were the only other parallel path than the current sharing factor would be determined by a comparison between the SQUID input reactance with $Z_{net} + Z_{com}$, and come to a factor of approximately 1.7. This path is unavoidable for any fMUX system, and its noise effects have been previously reported and accounted for.
3. Through parasitic capacitances to ground within the signal chain, including within SQUID card wiring, lithographic filters, and TES wafer, and returning through $R_{ref} = 0\ \Omega$. Together these impedances can be $\sim 20\ \Omega$ at the highest bias frequencies, making it a significant path through the system, primarily because it avoids the additional $\sim 10\ \Omega$ contribution from the wire-harness. This is possible because the ground inside the cryostat is intentionally well coupled to the ground outside the cryostat through structural and cryogenic elements, and because R_{ref} is low impedance. Once this path is included the current sharing factor jumps to over 2.5. This path exists only due to stray impedances in the system and is not fundamental. With this insight it can be engineered away.

A simplified schematic for these current paths is given in Figure 12. Current sharing was first noted in [4], where the second path above was identified. We now additionally identify the third path through the parasitic capacitance to ground as a major contribution to a high current sharing factor in SPT-3G.

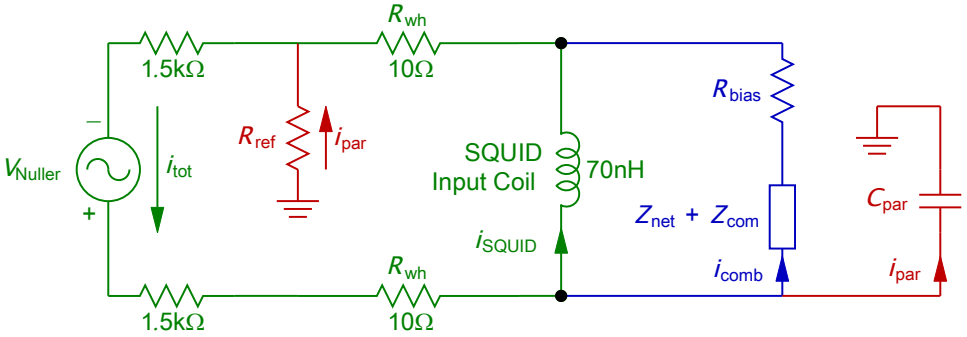

$$\text{Current Sharing Factor: } \frac{i_{tot}}{i_{SQUID}} = \frac{i_{SQUID} + i_{comb} + i_{par}}{i_{SQUID}}$$

Figure 12: A simplified diagram based on Figure 3, highlighting the different parallel paths for an input nuller current. Signals that require DAN to drive a current through the SQUID input coil will be shared between three possible current paths, shown in green, blue, and red. The green path is the intended outcome, the blue path is an inevitable source of current sharing due to the topology of fMUX systems, and the red path is due just to parasitic impedances in the system. Future receiver designs can mitigate this path with a re-engineering of a few electrical elements. The current sharing factor is the factor by which noise sources in the output path are amplified.

An exact calculation of the current sharing for each resonator requires a numerical simulation of the full circuit model, but the general form of the effect can be approximated by

$$\chi_{cs} = \frac{I_{\text{SQUID input coil}}}{I_{\text{Nuller input}}} \tag{14}$$

$$\approx \frac{((Z_{com}(\omega) + Z_{net}(\omega) + R_{wh})\, k\, j\omega L_{SQUID}) + R_{wh} + Z_{parasitic}}{Z_{parasitic}} \times \frac{j\omega L_{SQUID} + Z_{com}(\omega) + Z_{net}(\omega)}{Z_{com}(\omega_i) + Z_{net}(\omega)}, \tag{15}$$

for a $Z_{parasitic}$ that corresponds to the effective capacitive reactance of the parasitic current path. The current sharing factor is then given by $1/\chi_{cs}$.

6.1 In-situ current sharing model validation

A direct measurement of the current sharing factor is possible in-situ by comparing the amplitude of a known nuller input current to the signal measured at the SQUID output. Figure 13 shows the measured distribution of current sharing factor at each bias frequency in the SPT-3G system alongside a prediction based on the analytic circuit model.

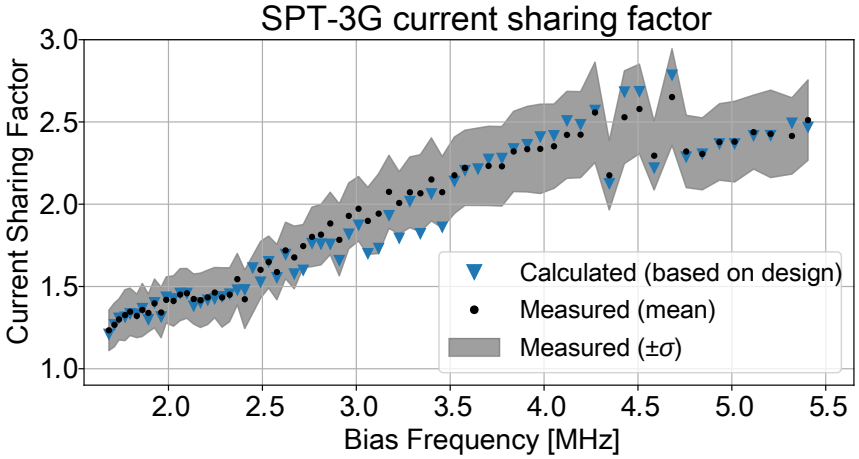

Figure 13: The current sharing factor ($1/\chi_{cs}$) can be measured directly in-situ and compared to an expectation based on an analytic evaluation of the electrical model shown in Figure 3, which includes both current sharing paths. The plot above compares the distribution of measured values for each detector across SPT-3G (mean and standard deviation, binned by resonator on the mux module) with a fully analytic expectation based on the readout design. The circuit simulation assumes designed values for all parameters, while the hardware in the receiver includes scatter in detector and filter properties, so width in the measured distribution is expected. The agreement between the simulations and measured values is excellent, and the largest disagreement corresponds to a known region of high scatter in the fabricated LC resonant frequencies, such that neighboring channels are more likely to deviate from the circuit model and have overlapping filters [5]. This suggests that an analytic model for the readout is accurately capturing the relevant dynamics for current sharing effects.

6.2 Experimental current sharing model validation

Although there are many relevant capacitances within the system, the return path for each of them flows through R_{ref}, which is currently a 0 Ω ground reference in the room-temperature electronics provided by a single resistor. The nuller input is transformer-coupled, and so this ground reference is required for the DC SQUID flux bias

(shown in Figure 3), but is not required to be low impedance. That choice was intended to prevent any ambient electromagnetic interference from generating voltages at the input of the SQUID, but the intent is undermined by enabling such a significant current sharing mechanismFigure 14 shows the simulated improvement in current sharing factor with R_{ref} =100 Ω. This model has been further validated by readout noise measurements conducted

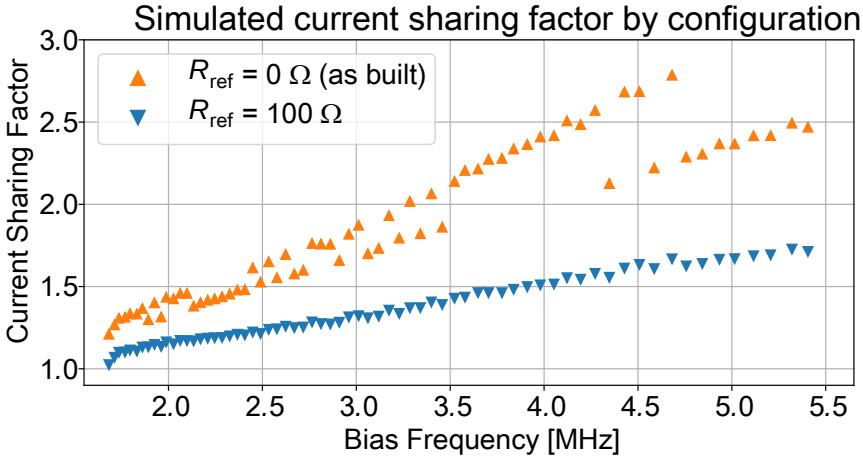

Figure 14: The low impedance ground reference allows a current sharing path through parasitic capacitances in the system, resulting in a substantial current sharing factor. Modifying this reference to increase the resistance to 100 Ω disables that current sharing path and improves the current sharing factor, as simulated above.By reducing the current sharing factor the noise performance of the system improves, as demonstrated in Figure 15.

in a laboratory testbed using 4 SQUID modules, shown in Figure 15The detectors and environment used for this test exhibit a slightly higher characteristic readout noise than seen on SPT-3G, but the significance of the noise improvement after the modification to R_{ref} is large relative to that difference, and consistent with expectations based on the predicted reduction in current sharing. At the highest frequencies, the noise improvement is more modest than expected, though this may be a consequence of the small number of detectors involved in the test or a feature of the laboratory test setup. It could also be indicating an additional current return point that remains uncharacterized, and warrants further investigation. This test demonstrates the utility of the readout model, which can reliably simulate changes in instrument performance as a function of design, and guide hardware changes to the electronics.

6.3 Potential benefit to SPT-3G

Modifying R_{ref} on existing room-temperature SPT-3G readout electronics could improve readout noise by up to ~35%, especially at high bias frequencies. Although such an intervention may take place during the next austral summer maintenance period, the overall improvement to the minimum variance CMB maps produced by SPT-3G would be small, and may not be worth the risk associated with hardware modification. Nevertheless, this change has been incorporated into the LiteBIRD readout design, where it substantially improves design margins for readout noise [5], and will be trialed on the updated Polarbear-2 receiver [19] in 2021.

7. CONCLUSION

The new generation of higher density and bandwidth DfMUX readout exercises the electronics signal paths in ways that previous generations did not. An extension of the analytic models used to predict crosstalk and noise performance is required to meet the needs of continued precision in forecasting and analysis of these systems. Presented here are new analytic formulas for crosstalk analysis, which better describe the SPT-3G performance, and a set of two previously unexplained mechanisms that were responsible for tensions between prior noise models

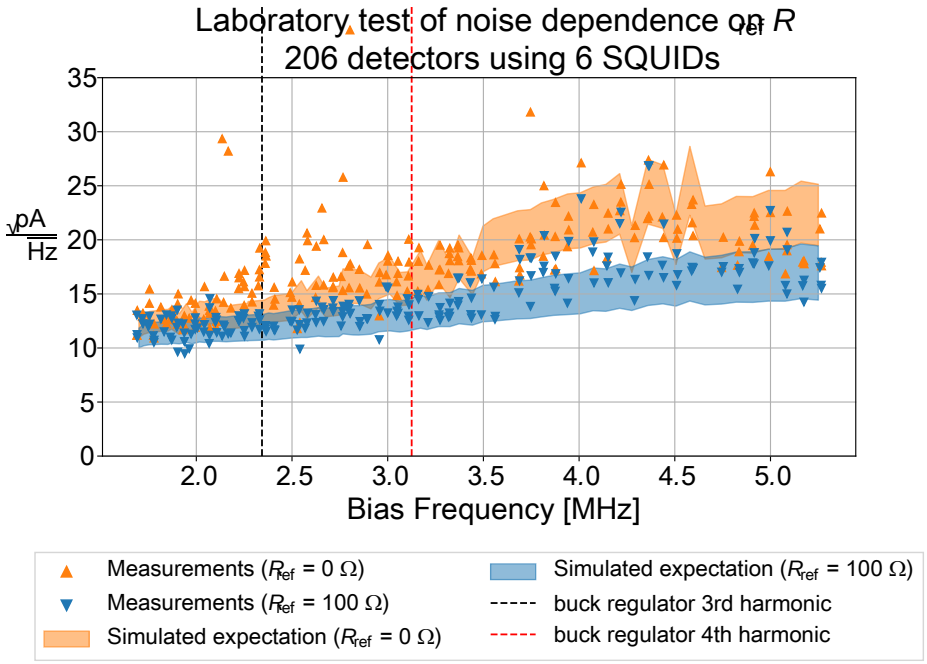

Figure 15: Laboratory tests of the modification to R_{ref} confirm that such a change substantially reduces readout noise.This improvement is consistent with a change in the current sharing factor as shown in Figure 14, although the highest frequency channels underperform expectations. This may be a feature of the small number of measurements made in a laboratory environment, but could also be indicating an additional current return point not yet characterized. Additionally, the modification improves scatter, particularly in channels near to the buck regulator frequencies, which suggests an improvement to the differential balancing and consequent electromagnetic inference susceptibility.

and measured readout noise performance.With this knowledge these noise mechanisms can be made negligible in future implementations.

ACKNOWLEDGMENTS

The South Pole Telescope program is supported by the National Science Foundation (NSF) through grant PLR-1248097.Partial support is also provided by the NSF Physics Frontier Center grant PHY-1125897 to the Kavli Institute of Cosmological Physics at the University of Chicago, the Kavli Foundation, and the Gordon and Betty Moore Foundation through grant GBMF#947 to the University of Chicago. Work at Argonne National Lab is supported by UChicago Argonne LLC, Operator of Argonne National Laboratory (Argonne). Argonne, a U.S. Department of Energy Office of Science Laboratory, is operated under contract no. DE-AC02-06CH11357. We also acknowledge support from the Argonne Center for Nanoscale Materials.Work at Fermi National Accelerator Laboratory, a DOE-OS, HEP User Facility managed by the Fermi Research Alliance, LLC, was supported under Contract No. DE-AC02-07CH11359. The McGill authors acknowledge funding from the Natural Sciences and Engineering Research Council of Canada, Canadian Institute for Advanced Research, and the Fonds de recherche du Qu´ebec Nature et technologies.N. Whitehorn acknowledges support from NSF CAREER grant AST-0956135. This manuscript was typeset using LaTeX, and formatted based on the SPIE style developed by Ken Hanson.[§] Many of the figures were made using matplotlib [20] and PGF/Tik Z [21]. Circuit diagrams were made using PyCirkuit, written by Orestes Mas. [¶] Numerical circuit simulations were performed using PySpice [22]Analyses were conducted using python scientific packages [23, 24, 25].

[§] https://kmh-lanl.hansonhub.com/spie/
[¶] https://github.com/orestesmas/pycirkuit

References

[1] Anderson, A. J., Ade, P. A. R., Ahmed, Z., Austermann, J. E., Avva, J. S., Barry, P. S., Thakur, R. B., Bender, A. N., Benson, B. A., Bleem, L. E., Byrum, K., Carlstrom, J. E., Carter, F. W., Cecil, T., Chang, C. L., Cho, H. M., Cliche, J. F., Crawford, T. M., Cukierman, A., Denison, E. V., de Haan, T., Ding, J., Dobbs, M. A., Dutcher, D., Everett, W., Foster, A., Gannon, R. N., Gilbert, A., Groh, J. C., Halverson, N. W., Harke-Hosemann, A. H., Harrington, N. L., Henning, J. W., Hilton, G. C., Holder, G. P., Holzapfel, W. L., Huang, N., Irwin, K. D., Jeong, O. B., Jonas, M., Khaire, T., Knox, L., Kofman, A. M., Korman, M., Kubik, D., Kuhlmann, S., Kuklev, N., Kuo, C. L., Lee, A. T., Leitch, E. M., Lowitz, A. E., Meyer, S. S., Michalik, D., Montgomery, J., Nadolski, A., Natoli, T., Nguyen, H., Noble, G. I., Novosad, V., Padin, S., Pan, Z., Pearson, J., Posada, C. M., Rahlin, A., Reichardt, C. L., Ruhl, J. E., Saunders, L. J., Sayre, J. T., Shirley, I., Shirokoff, E., Smecher, G., Sobrin, J. A., Stark, A. A., Story, K. T., Suzuki, A., Tang, Q. Y., Thompson, K. L., Tucker, C., Vale, L. R., Vanderlinde, K., Vieira, J. D., Wang, G., Whitehorn, N., Yefremenko, V., Yoon, K. W., and Young, M. R., "SPT-3G: A Multichroic Receiver for the South Pole Telescope," *Journal of Low Temperature Physics* **193**, 1057–1065 (Dec. 2018).

[2] Irwin, K. D. and Hilton, G. C., [*Transition-Edge Sensors*], vol. 99, 63 (2005).

[3] Dobbs, M., Bissonnette, E., and Spieler, H., "Digital Frequency Domain Multiplexer for Millimeter-Wavelength Telescopes," *IEEE Transactions on Nuclear Science* **55**, 21–26 (Jan. 2008).

[4] Bender, A. N., Anderson, A. J., Avva, J. S., Ade, P. A. R., Ahmed, Z., Barry, P. S., Basu Thakur, R., Benson, B. A., Bryant, L., Byrum, K., Carlstrom, J. E., Carter, F. W., Cecil, T. W., Chang, C. L., Cho, H. M., Cliche, J. F., Cukierman, A., de Haan, T., Denison, E. V., Ding, J., Dobbs, M. A., Dutcher, D., Everett, W., Ferguson, K. R., Foster, A., Fu, J., Gallicchio, J., Gambrel, A. E., Gardner, R. W., Gilbert, A., Groh, J. C., Guns, S., Guyser, R., Halverson, N. W., Harke-Hosemann, A. H., Harrington, N. L., Henning, J. W., Hilton, G. C., Holzapfel, W. L., Howe, D., Huang, N., Irwin, K. D., Jeong, O. B., Jonas, M., Jones, A., Khaire, T. S., Kofman, A. M., Korman, M., Kubik, D. L., Kuhlmann, S., Kuo, C. L., Lee, A. T., Leitch, E. M., Lowitz, A. E., Meyer, S. S., Michalik, D., Montgomery, J., Nadolski, A., Natoli, T., Nguyen, H., Noble, G. I., Novosad, V., Padin, S., Pan, Z., Paschos, P., Pearson, J., Posada, C. M., Quan, W., Rahlin, A., Riebel, D., Ruhl, J. E., Sayre, J. T., Shirokoff, E., Smecher, G., Sobrin, J. A., Stark, A. A., Stephen, J., Story, K. T., Suzuki, A., Thompson, K. L., Tucker, C., Vale, L. R., Vanderlinde, K., Vieira, J. D., Wang, G., Whitehorn, N., Yefremenko, V., Yoon, K. W., and Young, M. R., "On-Sky Performance of the SPT-3G Frequency-Domain Multiplexed Readout," *Journal of Low Temperature Physics* **199**, 182–191 (Apr. 2020).

[5] Montgomery, J., *Digital Frequency Domain Multiplexing readout: design and performance of the SPT-3G instrument and LiteBIRD satellite readout*, PhD thesis, McGill University (2020).

[6] Bender, A. N., Ade, P. A. R., Anderson, A. J., Avva, J., Ahmed, Z., Arnold, K., Austermann, J. E., Basu Thakur, R., Benson, B. A., Bleem, L. E., Byrum, K., Carlstrom, J. E., Carter, F. W., Chang, C. L., Cho, H. M., Cliche, J. F., Crawford, T. M., Cukierman, A., Czaplewski, D. A., Ding, J., Divan, R., de Haan, T., Dobbs, M. A., Dutcher, D., Everett, W., Gilbert, A., Groh, J. C., Guyser, R., Halverson, N. W., Harke-Hosemann, A., Harrington, N. L., Hattori, K., Henning, J. W., Hilton, G. C., Holzapfel, W. L., Huang, N., Irwin, K. D., Jeong, O., Khaire, T., Korman, M., Kubik, D., Kuo, C. L., Lee, A. T., Leitch, E. M., Lendinez, S., Meyer, S. S., Miller, C. S., Montgomery, J., Nadolski, A., Natoli, T., Nguyen, H., Novosad, V., Padin, S., Pan, Z., Pearson, J., Posada, C. M., Rahlin, A., Reichardt, C. L., Ruhl, J. E., Saliwanchik, B. R., Sayre, J. T., Shariff, J. A., Shirley, I., Shirokoff, E., Smecher, G., Sobrin, J., Stan, L., Stark, A. A., Story, K., Suzuki, A., Tang, Q. Y., Thompson, K. L., Tucker, C., Vanderlinde, K., Vieira, J. D., Wang, G., Whitehorn, N., Yefremenko, V., and Yoon, K. W., "Integrated performance of a frequency domain multiplexing readout in the SPT-3G receiver," in [*Millimeter, Submillimeter, and Far-Infrared Detectors and Instrumentation for Astronomy VIII*], Holland, W. S. and Zmuidzinas, J., eds., *Society of Photo-Optical Instrumentation Engineers (SPIE) Conference Series* **9914**, 99141D (July 2016).

[7] Bender, A. N., Ade, P. A. R., Ahmed, Z., Anderson, A. J., Avva, J. S., Aylor, K., Barry, P. S., Basu Thakur, R., Benson, B. A., Bleem, L. S., Bocquet, S., Byrum, K., Carlstrom, J. E., Carter, F. W., Cecil,

T. W., Chang, C. L., Cho, H. M., Cliche, J. F., Crawford, T. M., Cukierman, A., de Haan, T., Denison, E. V., Ding, J., Dobbs, M. A., Dodelson, S., Dutcher, D., Everett, W., Foster, A., Gallicchio, J., Gilbert, A., Groh, J. C., Guns, S. T., Halverson, N. W., Harke-Hosemann, A. H., Harrington, N. L., Henning, J. W., Hilton, G. C., Holder, G. P., Holzapfel, W. L., Huang, N., Irwin, K. D., Jeong, O. B., Jonas, M., Jones, A., Khaire, T. S., Knox, L., Kofman, A. M., Korman, M., Kubik, D. L., Kuhlmann, S., Kuo, C. L., Lee, A. T., Leitch, E. M., Lowitz, A. E., Meyer, S. S., Michalik, D., Montgomery, J., Nadolski, A., Natoli, T., Ngyuen, H., Noble, G. I., Novosad, V., Padin, S., Pan, Z., Pearson, J., Posada, C. M., Quan, W., Raghunathan, S., Rahlin, A., Reichardt, C. L., Ruhl, J. E., Sayre, J. T., Shirokoff, E., Smecher, G., Sobrin, J. A., Stark, A. A., Story, K. T., Suzuki, A., Thompson, K. L., Tucker, C., Vale, L. R., Vand erlinde, K., Vieira, J. D., Wang, G., Whitehorn, N., Wu, W. L. K., Yefremenko, V., Yoon, K. W., and Young, M. R., "Year two instrument status of the SPT-3G cosmic microwave background receiver," in [*Millimeter, Submillimeter, and Far-Infrared Detectors and Instrumentation for Astronomy IX*], Zmuidzinas, J. and Gao, J.-R., eds., *Society of Photo-Optical Instrumentation Engineers (SPIE) Conference Series* **10708**, 1070803 (July 2018).

[8] de Haan, T., Smecher,G., and Dobbs, M., "Improved performance of TES bolometers using digital feedback," in [*Millimeter, Submillimeter, and Far-Infrared Detectors and Instrumentation for Astronomy VI*], Holland, W. S. and Zmuidzinas, J., eds., *Society of Photo-Optical Instrumentation Engineers (SPIE) Conference Series* **8452**, 84520E (Sept. 2012).

[9] Hattori, K., Akiba, Y., Arnold, K., Barron, D., Bender, A., Dobbs, M. A., de Haan, T., Harrington, N., Hasegawa, M., Hazumi, M., Holzapfel, W. L., Hori, Y., Keating, B. G., Lee, A. T., Montgomery, J., Morii, H., Myers, M. J., Rotermund, K., Shirley, I., Smecher, G. M., Stebor, N., Suzuki, A., and Tomaru, T., "Optimization of cold resonant filters for frequency domain multiplexed readout of POLARBEAR-2," in [*Millimeter, Submillimeter, and Far-Infrared Detectors and Instrumentation for Astronomy VII*], Holland, W. S. and Zmuidzinas, J., eds., *Society of Photo-Optical Instrumentation Engineers (SPIE) Conference Series* **9153**, 91531B (Aug. 2014).

[10] Rotermund, K., Barch, B., Chapman, S., Hattori, K., Lee, A., Palaio, N., Shirley, I., Suzuki, A., and Tran, C., "Planar Lithographed Superconducting LC Resonators for Frequency-Domain Multiplexed Readout Systems," *Journal of Low Temperature Physics* **184**, 486–491 (July 2016).

[11] Dutcher, D., Ade, P. A. R., Ahmed, Z., Anderson, A. J., Avva, J. S., Thakur, R. B., Bender, A. N., Benson, B. A., Carlstrom, J. E., Carter, F. W., Cecil, T. W., Chang, C. L., Cliche, J. F., Cukierman, A., de Haan, T., Ding, J., Dobbs, M. A., Everett, W., Foster, A., Gallicchio, J., Gilbert, A., Groh, J. C., Harke-Hosemann, A. H., Guns, S. T., Halverson, N. W., Harrington, N. L., Henning, J. W., Holzapfel, W. L., Huang, N., Irwin, K. D., Jeong, O. B., Jonas, M., Khaire, T. S., Kofman, A. M., Korman, M., Kubik, D. L., Kuhlmann, S., Kuo, C. L., Lowitz, A. E., Lee, A. T., Meyer, S. S., Michalik, D., Montgomery, J., Nadolski, A., Natoli, T., Nguyen, H., Noble, G. I., Novosad, V., Padin, S., Pan, Z., Pearson, J., Posada, C. M., Quan, W., Rahlin, A., Ruhl, J. E., Sayre, J. T., Shirokoff, E., Smecher,G., Sobrin, J. A., Stark, A. A., Story, K. T., Suzuki, A., Thompson, K. L., Tucker, C., Vanderlinde, K., Vieira, J. D., Wang, G., Whitehorn, N., Yefremenko, V., Yoon, K. W., and Young, M. R., "Characterization and performance of the second-year SPT-3G focal plane," in [*Millimeter, Submillimeter, and Far-Infrared Detectors and Instrumentation for Astronomy IX*], Zmuidzinas, J. and Gao, J.-R., eds., *Society of Photo-Optical Instrumentation Engineers (SPIE) Conference Series* **10708**, 107081Z (July 2018).

[12] Elleflot, T., *Measuring the Polarization of the Cosmic Microwave Background with POLARBEAR-1 and Developing the Next-Generation Experiment POLARBEAR-2*, PhD thesis, UC, San Diego (2019).

[13] Avva, J. S., Ade, P. A. R., Ahmed, Z., Anderson, A. J., Austermann, J. E., Thakur, R. B., Barron, D., Bender, A. N., Benson, B. A., Carlstrom, J. E., Carter, F. W., Cecil, T., Chang, C. L., Cliche, J. F., Cukierman, A., Denison, E. V., de Haan, T., Ding, J., Dobbs, M. A., Dutcher, D., Elleflot, T., Everett, W., Foster, A., Gannon, R. N., Gilbert, A., Groh, J. C., Halverson, N. W., Harke-Hosemann, A. H., Harrington, N. L., Hasegawa,M., Hattori, K., Henning, J. W., Hilton, G. C., Holzapfel, W. L., Hori, Y., Huang, N., Irwin, K. D., Jeong, O. B., Jonas, M., Khaire, T., Kofman, A. M., Korman, M., Kubik, D., Kuhlmann, S., Kuo, C. L., Lee, A. T., Lowitz, A. E., Meyer, S. S., Montgomery, J., Nadolski, A., Natoli, T., Nguyen,

H., Nishino, H., Noble, G. I., Novosad, V., Padin, S., Pan, Z., Pearson, J., Posada, C. M., Rahlin, A., Rotermund, K., Ruhl, J. E., Saunders, L. J., Sayre, J. T., Shirley, I., Shirokoff, E., Smecher, G., Sobrin, J. A., Stark, A. A., Story, K. T., Suzuki, A., Tang, Q. Y., Thompson, K. L., Tucker, C., Vale, L. R., Vanderlinde, K., Vieira, J. D., Wang, G., Whitehorn, N., Yefremenko, V., Yoon, K. W., and Young, M. R., "Design and Assembly of SPT-3G Cold Readout Hardware," *Journal of Low Temperature Physics* **193**, 547–555 (Nov. 2018).

[14] Dobbs, M. A., Lueker, M., Aird, K. A., Bender, A. N., Benson, B. A., Bleem, L. E., Carlstrom, J. E., Chang, C. L., Cho, H. M., Clarke, J., Crawford, T. M., Crites, A. T., Flanigan, D. I., de Haan, T., George, E. M., Halverson, N. W., Holzapfel, W. L., Hrubes, J. D., Johnson, B. R., Joseph, J., Keisler, R., Kennedy, J., Kermish, Z., Lanting, T. M., Lee, A. T., Leitch, E. M., Luong-Van, D., McMahon, J. J., Mehl, J., Meyer, S. S., Montroy, T. E., Padin, S., Plagge, T., Pryke, C., Richards, P. L., Ruhl, J. E., Schaffer, K. K., Schwan, D., Shirokoff, E., Spieler, H. G., Staniszewski, Z., Stark, A. A., Vanderlinde, K., Vieira, J. D., Vu, C., Westbrook, B., and Williamson, R., "Frequency multiplexed superconducting quantum interference device readout of large bolometer arrays for cosmic microwave background measurements," *Review of Scientific Instruments* **83**, 073113–073113–24 (July 2012).

[15] Zmuidzinas, J., "Thermal noise and correlations in photon detection," *Applied Optics* **42**, 4989–5008 (Sept. 2003).

[16] Mather, J. C., "Bolometer noise: nonequilibrium thoery," *Applied Optics* **21**, 1125–1129 (Mar. 1982).

[17] Lueker, M., *Measurements of Secondary Cosmic Microwave Background Anisotropies with the South Pole Telescope*, PhD thesis, University of California, Berkeley (2010).

[18] J. Clarke, A. B., [*The SQUID Handbook: Fundamentals and Technology of SQUIDs and SQUID Systems*], vol. 1, Wiley-VCH Verlag GmbH & Co. KGa (2004).

[19] Tomaru, T., Hazumi, M., Lee, A. T., Ade, P., Arnold, K., Barron, D., Borrill, J., Chapman, S., Chinone, Y., Dobbs, M., Errard, J., Fabbian, G., Ghribi, A., Grainger, W., Halverson, N., Hasegawa, M., Hattori, K., Holzapfel, W. L., Inoue, Y., Ishii, S., Kaneko, Y., Keating, B., Kermish, Z., Kimura, N., Kisner, T., Kranz, W., Matsuda, F., Matsumura, T., Morii, H., Myers, M. J., Nishino, H., Okamura, T., Quealy, E., Reichardt, C. L., Richards, P. L., Rosen, D., Ross, C., Shimizu, A., Sholl, M., Siritanasak, P., Smith, P., Stebor, N., Stompor, R., Suzuki, A., Suzuki, J.-i., Takada, S., Tanaka, K.-i., and Zahn, O., "The POLARBEAR-2 experiment," in [*Millimeter, Submillimeter, and Far-Infrared Detectors and Instrumentation for Astronomy VI*], Holland, W. S. and Zmuidzinas, J., eds., *Society of Photo-Optical Instrumentation Engineers (SPIE) Conference Series* **8452**, 84521H (Sept. 2012).

[20] Hunter, J. D., "Matplotlib: A 2D Graphics Environment," *Computing in Science and Engineering* **9**, 90–95 (May 2007).

[21] Tantau, T., *The TikZ and PGF Packages: Manual for version 3.0.0*. http://sourceforge.net/projects/pgf/.

[22] Salvaire, F., "Pyspice." https://pyspice.fabrice-salvaire.fr (2019).

[23] Virtanen, P., Gommers, R., Oliphant, T. E., Haberland, M., Reddy, T., Cournapeau, D., Burovski, E., Peterson, P., Weckesser, W., Bright, J., van der Walt, S. J., Brett, M., Wilson, J., Jarrod Millman, K., Mayorov, N., Nelson, A. R. J., Jones, E., Kern, R., Larson, E., Carey, C., Polat, İ., Feng, Y., Moore, E. W., Vand erPlas, J., Laxalde, D., Perktold, J., Cimrman, R., Henriksen, I., Quintero, E. A., Harris, C. R., Archibald, A. M., Ribeiro, A. H., Pedregosa, F., van Mulbregt, P., and Contributors, S. . ., "SciPy 1.0: Fundamental Algorithms for Scientific Computing in Python," *Nature Methods* **17**, 261–272 (2020).

[24] van der Walt, S., Colbert, S. C., and Varoquaux, G., "The numpy array: A structure for efficient numerical computation," *Computing in Science Engineering* **13**(2), 22–30 (2011).

[25] Perez, F. and Granger, B. E., "Ipython: A system for interactive scientific computing," *Computing in Science Engineering* **9**(3), 21–29 (2007).